

An Overview of the U.S. Army Aviation Development Directorate Quadrotor Guidance, Navigation, and Control Project

Kenny K. Cheung
Joseph A. Wagster IV
Universities Space Research
Association
U.S. Army Aviation
Development Directorate
(AMRDEC)
NASA Ames Research Center
Moffett Field, CA

Mark B. Tischler
Christina M. Ivler
Marcos G. Berrios
Tom Berger
U.S. Army Aviation
Development Directorate
(AMRDEC)
Moffett Field, CA

Ondrej Juhasz
Eric L. Tobias
Chad L. Goerzen
Patrick S. Barone
Frank C. Sanders
Mark J. S. Lopez
San Jose State University
U.S. Army Aviation
Development Directorate
(AMRDEC)
Moffett Field, CA

Rhys M. Lehmann
Defence Science and
Technology Group
Melbourne, Australia

ABSTRACT

In recent years, there has been growing commercial and military interest in small-scale multi-rotor unmanned aerial systems (UAS), from commercial package delivery, to performing search and rescue missions, to providing surveillance and reconnaissance support. The Vehicle Management and Control (VMC) Technical Area under the U.S. Army Aviation Development Directorate (ADD) at Moffett Field, California has strong experience and expertise in applying advanced flight control and obstacle field navigation (OFN) technologies to full-size manned and unmanned rotorcraft. The Quadrotor Guidance, Navigation, and Control project was established to develop and apply these advanced technologies to a small-scale commercial-off-the-shelf (COTS) multi-rotor UAS to support emerging Department of Defense and industry needs. This paper provides an overview of the project, from the organizational aspect, to the development of the hardware and software infrastructure, to the application of the aforementioned advanced technologies to a 3D Robotics IRIS+ quadrotor research vehicle. Example results for each core technology component (system identification, flight control design and optimization, hardware-in-the-loop simulation, flight testing and validation) are presented to demonstrate its successful application to the IRIS+. Current work in developing scoring metrics and scaled ADS-33 Mission Task Elements (MTEs) for evaluating the performance of control designs based on aggressiveness, tracking, and robustness are discussed. Recent development of a quadrotor-specific Control Equivalent Turbulence Input (CETI) turbulence model and its application in the design of a performance-based disturbance rejection flight control system are also summarized.

NOTATION

A, B, C, D	State-space representation	COA	Certificate of Waiver or Authorization
ACAH	Attitude-Command/Attitude-Hold	CETI	Control Equivalent Turbulence Input
ADD	Aviation Development Directorate	CIFER [®]	Comprehensive Identification from Frequency Responses software
CAF	Cable Angle/Rate Feedback	CONDUIT [®]	Control Designer's Unified Interface software

Presented at the AHS International 73rd Annual Forum & Technology Display, Fort Worth, Texas, USA, May 9-11, 2017. This is a work of the U.S. Government and is not subject to copyright protection in the U.S.

DISTRIBUTION A. Approved for public release: distribution unlimited.

CR	Cramér-Rao bounds
DEP	Distributed Electrical Propulsion
DI	Dynamic Inversion architecture
DMO	Design Margin Optimization
DRB	Disturbance Rejection Bandwidth [rad/sec]
DRP	Disturbance Rejection Peak [dB]
EMF	Explicit Model Following architecture
FTUAS	Future Tactical Unmanned Aerial Systems
GM	Gain margin [dB]
HIL	Hardware-in-the-loop
IMU	Inertial Measurement Unit
J_{ave}	Average cost for frequency response error
L	Scoring objective function
L_p	Roll damping stability derivative
L_{path}	Maximum commanded distance from starting point of the trajectory [ft]
L_v	Roll stability derivative
$L_{\delta_{lat}}$	Lateral mixer control derivative
lat	Lateral axis lag frequency [rad/sec]
LIDAR	Light Detection and Ranging
MTE	Mission Task Element
$N_{flights}$	Number of flights
$N_{success}$	Number of successful flights
OFN	Obstacle Field Navigation
p	Vehicle roll rate [rad/sec]
PH	Position Hold
PM	Phase margin [deg]
pos	Position error along trajectory [ft]
q	Vehicle pitch rate [rad/sec]
R	Robustness scoring metric
r	Vehicle yaw rate [rad/sec]
RIPTIDE	Real-time Interactive Prototype Technology Integration/Development Environment
RMS	Root Mean Square
RMSE	Root-Mean-Square Error
SIL	Software-in-the-loop
UAS	Unmanned Aerial Systems
UAV	Unmanned Aerial Vehicle
V	Velocity along scaled trajectory [ft/sec]
v	Lateral velocity [ft/sec]
vel	Velocity error along trajectory [ft/sec]
VFD	Variable Frequency Drive
VMC	Vehicle Management and Control
VTOL	Vertical Take-off and Landing
w	Weight for scoring metrics
x	Longitudinal position [ft]
y	Lateral position [ft]
Y_v	Lateral speed damping stability derivative
α	Aggressiveness scoring metric
δ	Commanded input
ε	Tracking error
ψ	Vehicle yaw angle [deg]
Φ	Final maneuver score
ϕ	Vehicle roll angle [deg]
τ	Time delay [sec]
τ_{double}	Time to double for unstable mode [sec]

θ	Vehicle pitch angle [deg]
ω	Frequency [rad/sec]
ω_c	Crossover frequency [rad/sec]

Subscripts

B	Bad scoring metric value
c	Commanded input
d	Disturbance
err	Attitude/position error
G	Good scoring metric value
lat	Lateral axis
lon	Longitudinal axis
m	Measured
max,cmd	Maximum commanded
nom	Unscaled trajectory
ped	Directional axis
$pilot$	Piloted command
t	Turbulence input

Superscripts

'	Total command downstream of disturbance
---	---

INTRODUCTION

Over the past few years, there has been widespread commercial and military interest in small/nano battery-powered multi-rotor unmanned aerial systems (UAS). The U.S. Army Unmanned Aircraft Systems Roadmap 2010-2035 (Ref. 1) refers to this smallest category of UAS as “Group 1” (less than 20 lb). A key motivation for the adoption of the battery-powered quadrotor configuration is the simplicity and high reliability due to the few number of moving parts. While quadrotor configurations are widely adopted, “multi-rotor” concepts with additional rotor systems allow for redundancy and failure reconfiguration. Another advantage of the battery-powered quad- or multi-rotor is that the rotor thrust is controlled by RPM, which has a very high rate of response due to large torque capability of the electric motor, effectively eliminating actuator rate limiting (a common limitation on full-size rotorcraft). Electric motors are extremely compact and self-contained, allowing for many new configuration designs with various combinations of multiple rotors (and wings) that are carefully optimized for their intended market/application. Finally, and especially important for military applications, the small quadrotors have much lower noise levels as compared to the full-size conventional rotorcraft, and their noise level can hardly be distinguished from the ambient noise beyond 100 to 200 ft in altitude (Ref. 2).

Commercial quadrotor applications in the small-size (Group 1) market include real-time aerial video for news, filmmaking, fire/police support, and agricultural mapping. Commercial multi-rotor configurations in the Group 1 category are also in development for cargo delivery in several high-profile efforts by DHL (“Parcelcopter”) and Google-X

(“Project Wing”). A recently announced effort by UPS would launch a ten-pound (Group 1) package delivery octocopter from a UPS truck, for up to a five-pound payload and flight speeds of up to 22 mph (Ref. 3), as shown in Figure 1. Finally, the Amazon “Prime Air” package delivery multi-rotor configuration is anticipated to be heavier (55 lb), within the Department of Defense (DoD) Group 2 category (21 to 55 lb).



Figure 1. UPS package delivery using an octocopter.
(Photo: UPS)

The U.S. DoD (DARPA) Fast Lightweight Autonomy Program (FLA) has demonstrated autonomous indoor maneuvering flight without GPS on a commercial quadrotor (Group 1) at speeds of up to 45 mph. Commercial quadrotors with specialized modifications are also being used by insurgent forces with deadly effect. For instance, the DJI Phantom 4 Falcon series have been equipped with grenades and explosive shells and fielded for attacks in Mosul, as reported and captured on video by CBS News (Ref. 4) and in an online article recently published by BBC News (Figure 2, Ref. 5).

Engineering model-based flight control design and development methods are standard in the development of full-size manned and unmanned rotorcraft flight dynamics and control. Yet, these methods are not widely used for small UAS development, which rely more commonly on hand-tuning of the flight control systems that will not provide an optimal flight dynamics and control solution. Some research efforts have been recently published that demonstrate the effectiveness of the engineering methods for small UAS applications, including quadrotor configurations. Niermeyer, Raffler, and Holzapfel (Ref. 6) used CIPHER[®] (Comprehensive Identification from Frequency Responses) frequency-domain system identification methods (Ref. 7) to determine a flight dynamics model of the AscTec Hummingbird quadcopter (1.6 lb, Group 1). In a collaborative research effort between the University of Cincinnati and the U.S. Army Aviation Development Directorate (ADD) at Moffett Field, California

(Ref. 8), CIPHER[®] frequency-domain system identification and CONDUIT[®] (Control Designer's Unified Interface) optimization-based flight control design techniques (Ref. 9) were applied to the flight control development of an AeroQuad Cyclone quadrotor. Optimized flight response characteristics were much improved as compared to the stock system. System identification studies of the IRIS+ quadrotor (also used herein) were documented by Cooper et al. (Ref. 10).



Figure 2. Weaponized commercial quadrotor.
(Photo: Mitch Utterback)

The Vehicle Management and Control (VMC) Technical Area under ADD has a strong technology base and expertise in advanced flight dynamics and control technologies applied to many *full-size* manned and unmanned conventional rotorcraft, as well as the *mid-size* RMAX UAV helicopter (160 lb, Group 3). These technologies include the development of ADS-33 handling qualities requirements (Ref. 11), CIPHER[®] system identification methods for rapid/accurate simulation model determination, flight control validation, and hardware-in-the-loop testing (Ref. 7), and CONDUIT[®] optimization-based flight control design methods (Ref. 9). When integrated into the full-size rotorcraft development programs, these technologies ensure efficient and safe development and flight-testing of operationally effective (manned and unmanned) rotorcraft. Guidance technologies for practical obstacle field navigation have been successfully demonstrated using real-time measurements for the RMAX UAV helicopter and, most recently, for the UH-60 helicopter (Ref. 12). The ADD at Moffett Field has established the Quadrotor Guidance, Navigation, and Control project to develop, assess, adapt, and document advanced flight control technologies for application to small-scale quadcopters. These methods will be applicable to other multi-

rotor VTOL UAS in this class to support emerging DoD and industry interest.

This paper provides an overview of the Quadrotor Guidance, Navigation, and Control (GNC) project. The paper describes how the project has been organized, what hardware and software are used, and provides example flight test results for the chosen research vehicle platform (3D Robotics IRIS+, Ref. 13). The paper also highlights the “desktop-to-flight” development workflow developed by ADD, and how this workflow and associated engineering methodologies are adapted to small-scale rotorcraft like quadrotors. Each component of the workflow and the associated tool applied is explained. System identification modeling, flight control design, and flight-testing results are highlighted from indoor and outdoor experiments. Previous results under this project have been published by Juhasz et al. (Ref. 14), wherein a Control Equivalent Turbulence Input (CETI) model was identified for the research vehicle. This work will be briefly summarized in a later section of the paper.

PROJECT OVERVIEW

The Quadrotor Guidance, Navigation, and Control project consists of two development phases. In Phase 1, the goal is to develop the necessary research infrastructures and to build up experience with adapting flight control technologies from full-scale vehicles to a small-scale vehicle. As part of the overall project challenge, it was determined at an early stage that alternative control law architectures would be designed and applied to the quadrotor using different control optimization strategies, instead of simply re-using and re-tuning the conventional PID controllers found in many commercial off-the-shelf (COTS) quadrotor vehicles. Therefore, the project team was divided into two groups to design the control laws. Due to the extensive approval process required in obtaining a Certificate of Waiver or Authorization (COA) from the FAA for flying outdoor within the Moffett Federal Airfield, the primary focus in Phase 1 was to develop and validate the inner-loop control law designs based on indoor flight tests conducted at indoor testing facilities at Ames Research Center. In Phase 2, the outer-loop control laws will be designed and flight-tested outdoor at Moffett Federal Airfield and other approved test sites at Ames. As part of the research activities, re-scaled ADS-33 flight missions that are applicable to the small UAS will be defined. Inspired by the “Design, Construction, and Testing of Autonomous Aircraft” course offered by the Department of Aeronautics and Astronautics at Stanford University, mission-based scoring and benchmarking metrics for evaluating and grading the performance of the control law designs are being formulated. Phase 2 will conclude with an outdoor flight demonstration event, where the capability of the designs in meeting the defined flight missions will be showcased. Each design will be evaluated and scored based on the defined performance metrics for each flight task at the event.

The project was initiated in late 2014, when many inexpensive ready-to-fly (RTF) quadrotor vehicles on the market were assessed, and the 3D Robotics IRIS+ (Ref. 13) was down-selected as the target research vehicle platform due to the relative simplicity of the airframe, the open-source flight software that allows for easy customization, and the low overall cost of the system. Phase 1 was successfully completed in late 2015. Two different control law architectures, Explicit Model Following (EMF) and Dynamic Inversion (DI), both of which are commonly used in full-scale vehicles, were applied to the inner-loop control law design using different control optimization strategies. A hardware-in-the-loop simulation was developed to allow validation of flight software prior to flight tests. All developmental flight-testing and validation work for Phase 1 were conducted inside a hangar building at Ames Research Center. This phase was concluded with an indoor flight demonstration that showcased the achieved performance.

Recently, the project has transitioned to Phase 2. In addition to preparing for outdoor free flights, infrastructure to conduct outdoor tethered flights has been established so that initial flight tests and experiments can be conducted in a more controlled environment. As part of the project research activities, a turbulence model for the quadrotor, based on the Control Equivalent Turbulence Input (CETI) (Ref. 15, Ref. 16), was also developed (Ref. 14) in conjunction with a study on performance-based disturbance rejection for the quadrotor (Ref. 17). To support these research activities, a fan system has been developed to serve as the “turbulence arena” to generate turbulence which allows consistent assessment of the performance of the quadrotor vehicle to reject various levels of turbulence.

QUADROTOR HARDWARE AND INFRASTRUCTURE SETUP

IRIS+ Quadrotor System

The 3D Robotics IRIS+, as shown in Figure 3, is a quadrotor configuration that measures 550 mm diagonally, has a total flying weight of approximately 1700 g, a payload capacity of 400 g, and an endurance of approximately 16 min (Ref. 13). The aircraft features the open source Pixhawk flight computer running ArduPilot-based ArduCopter firmware (Ref. 13), and has ground control station capability to read real-time telemetry and upload data such as navigation waypoints or controller gains to the aircraft.

The ArduCopter firmware consists of many modules that cover each aspect of vehicle control. There are separate modules for navigation, telemetry, data recording, camera control, etc. Since the ArduCopter code base is written in C++, using MathWorks® code generation product, Embedded Coder®, a “pictures-to-code” process has been developed to generate C++ code for the advanced control laws developed

in Simulink® block diagram format to directly replace the stock IRIS+ control laws on-board the vehicle.

ArduCopter also features different flight modes such as “Loiter,” “Position Hold,” and “Stabilize,” and each mode has different requirements and usage of on-board sensors. The built-in ability to switch to different flight modes via a multi-position switch on the RC transmitter was utilized and configured to switch between the default “Stabilize” flight mode and the research flight modes. Moreover, for system identification purposes, additional data logging were added in the firmware to record at a higher frequency, and switches and knobs on the radio transmitter were also programmed to initiate auto-coded frequency sweep maneuvers for the various axes.



Figure 3. The 3D Robotics IRIS+.

Tether System

As part of the Phase 2 outdoor flight test setup, a tether system was developed so that the IRIS+ can be flown in a more controlled environment for basic hover and low-speed maneuvers. The tether system consists of a 90 ft long, 200 lb test Kevlar tether, a bungee cord, and a 20 lb kettlebell, as shown in Figure 4. The kettlebell acts as a mobile tether base, while the bungee cord gently absorbs energy should the pilot inadvertently reach the limits of the tether. Instead of a sharp jerk, the bungee allows for a gentle arrest of movement when the extremity is reached. The Kevlar tether is attached at four points of the aircraft for redundancy. The Kevlar tether was chosen due to its high strength-to-weight ratio, so the weight and dynamics of the tether are considered negligible and omitted from analysis.

Turbulence Arena

One of the Phase 2 research activities is to assess and quantify the disturbance rejection performance of the IRIS+. To demonstrate the disturbance rejection capability of the designed control laws in a realistic, controlled scenario, a high

mass flow rate fan system, or “turbulence arena,” was assembled. The fan system is comprised of a fan, a variable frequency drive (VFD), and a gasoline powered generator. The fan is 36 in. in diameter, has a flow rate of 1,810 ft³/min, and operates on three-phase 240V AC power. The gasoline-powered generator provides both single phase 240V AC and single phase 120V AC outputs. The VFD was used to convert the generator’s output to the three phase 240V AC power that the fan requires. The VFD also allows for fine control of the fan speed through variation of the drive frequency. To quantify the magnitude of the turbulence created by the fan system, an ultrasonic three-axis anemometer was used (Ref. 18). The anemometer has two sets of three ultrasonic pulse generators and receivers that are paired along the diagonals. The anemometer calculates the time associated with each pair and calculates the wind velocity components. The three velocity components, as well as azimuth and elevation, are all recorded at 32 Hz. The turbulence arena setup is shown in Figure 5.



Figure 4. Tether system.

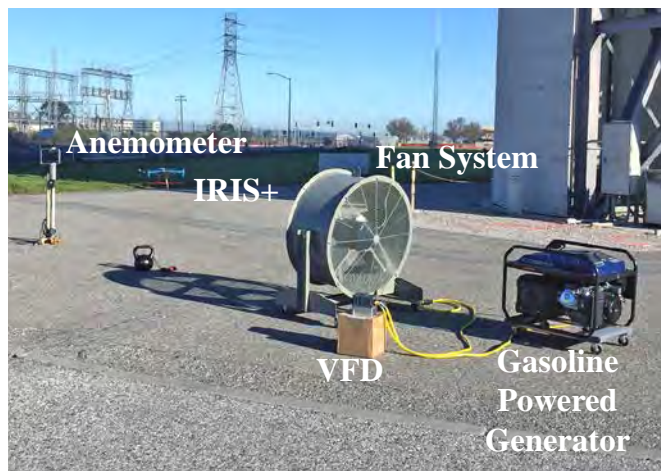


Figure 5. Turbulence arena setup.

LIDAR/Optical Flow Sensor System

To measure ground velocities alongside GPS derived ground velocities, a PX4FLOW optical flow sensor (Ref. 19) is used in conjunction with a Lidar-Lite Light Detection And Ranging sensor (LIDAR) (Ref. 20). The optical flow sensor scans for relative movement of ground features and textures in the sensor’s camera, and outputs forward and sideward velocities of the terrain. Given that the ground’s velocity relative to the aircraft varies with altitude, the LIDAR is used to sense the aircraft’s height above the ground and calibrate the optical flow velocity to the vehicle velocity. The LIDAR has a usable range of 40 m and is accurate to 1 cm. Additionally, there is an inertial measurement unit (IMU) mounted to the optical flow sensor circuit board that compensates for the body frame attitudes and their effect on the flow velocity measurement. A custom sensor mount was fabricated to mount the LIDAR and the optical flow sensor together securely on the bottom of the fuselage and as close to the center of gravity of the aircraft as possible. The mount and sensor package are shown in Figure 6.

software- and hardware-in-the-loop simulations, and flight-testing. Each element of the workflow must be carefully validated in order for the process to provide a design that performs as expected in flight. Implementation of such an integrated and validated workflow is the key to a good initial flight control system and an efficient iterative development process, which reduces the time and cost for flight testing and tuning. This workflow also allows for the evaluation of design trade-offs and the assessment of robustness to uncertainties to be effectively and safely addressed.

RESEARCH METHODS AND SAMPLE RESULTS

The “desktop-to-flight” development workflow was developed by ADD to support full-scale manned and unmanned flight control research and development (Ref. 9). As depicted in Figure 7, the development workflow has been adapted and modified to support the development of small-scale multi-rotor vehicles like the IRIS+. Key elements of the workflow include the development of flight dynamics simulation models using system identification methodologies, optimization-based control system design and analysis,

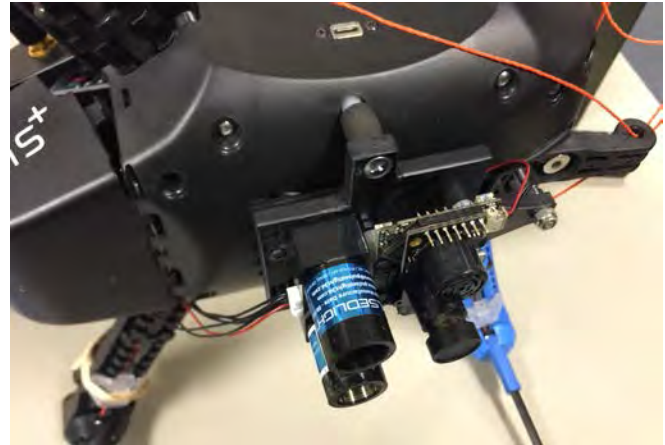


Figure 6. Sensor system mounted on the IRIS+.

In the following sections, the application of each component of the workflow and its associated tool to the Quadrotor GNC project is explained, and example results are presented.

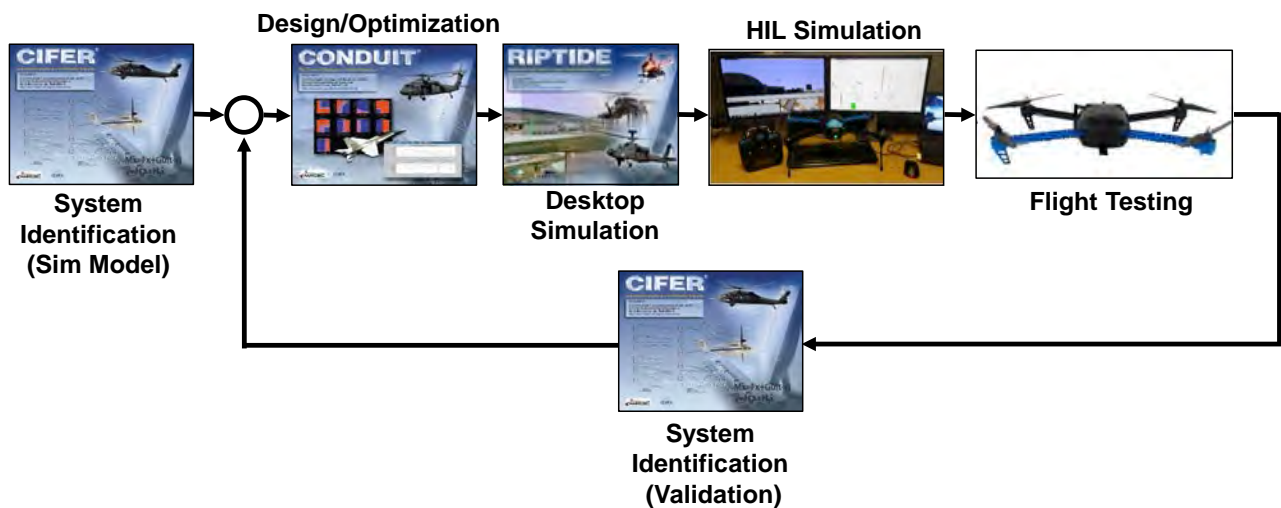


Figure 7. “Desktop-to-flight” development workflow (Adapted from Ref. 9).

Bare-Airframe System Identification

Prior to designing new control laws for the IRIS+, the first step in the development process was to obtain an accurate bare-airframe model of the vehicle, which contains the dynamics of the IRIS+ airframe, mixer, and motors, as shown in Figure 8. The frequency-domain-based system identification tool CIPHER[®] (Ref. 7) was used to extract frequency responses from flight data for state-space model identification as well as validation and analysis. In Phase 1 of the project, indoor flights were conducted inside a hangar building at Ames Research Center, which had adequate room for frequency sweep testing of the quadrotor dynamics in hover for all axes. As the project transitioned to Phase 2, frequency sweeps have also been conducted outdoors with the tether system in hover.

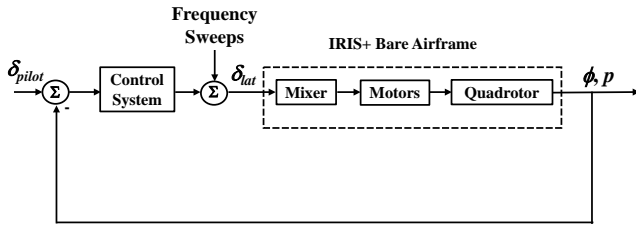


Figure 8. Schematic representation of the IRIS+ control system to illustrate location of frequency sweeps for bare-airframe identification.

Since the bare-airframe of the IRIS+ is inherently unstable, all data was collected with the control system engaged. Automated frequency sweeps as well as piloted 3-2-1-1 type inputs with additional high-frequency content were used to excite the aircraft. These inputs were inserted just upstream of the mixer to control the bare-airframe directly, as illustrated in Figure 8. Even with the control systems engaged, logging of the total mixer inputs enables identification of the bare-airframe dynamics (p/δ_{lat}). A sample time history of a lateral axis automated frequency sweep is shown in Figure 9. Note that the spikes in the mixer input and roll rate come from piloted inputs being added on top of the automated sweep to prevent large drifts and maintain the response centered around the hover flight condition.

The frequency range of interest for control design is based on the controller crossover frequency, ω_c (Ref. 7):

$$0.3 \omega_c \leq \omega \leq 3 \omega_c \quad (1)$$

The inner stabilizing loop of the IRIS+ stock control system (“Stabilize” mode) has a crossover frequency (ω_c) of around 20 to 30 rad/sec in the lateral and longitudinal axes, which is an order of magnitude greater than most conventional manned aircraft and rotorcraft. Therefore, modeled dynamics must extend to at least 60 rad/sec in these axes according to Eq. 1. On the other hand, the crossover

frequencies in the heave and directional axes are lower at around 6 rad/sec for directional axis and 10 rad/sec for the heave axis, respectively, so the excitation of the bare-airframe was not extended to such high frequencies for these axes.

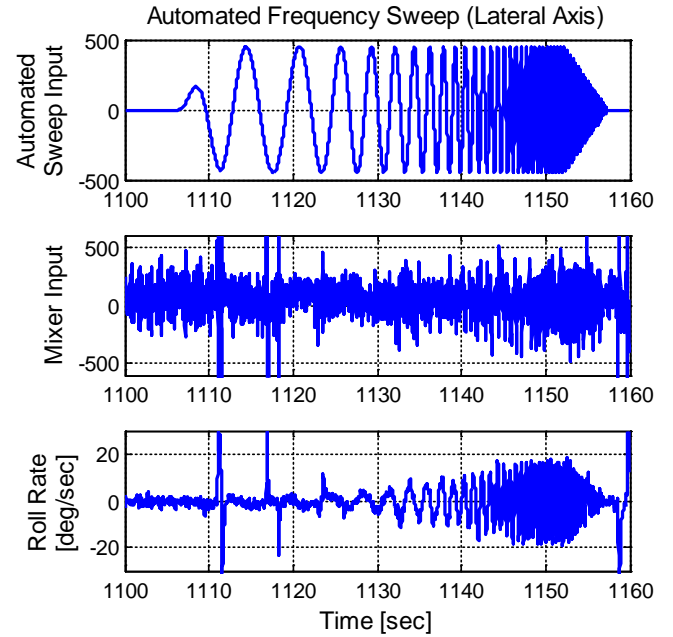


Figure 9. Sample time history of lateral axis automated frequency sweep.

The bare-airframe identification model structure and results align well with those previously published (Ref. 6, Ref. 8). A total of 15 states were required to model the full aircraft, including the 9 rigid-body states as well as high-frequency “lags.” The lags represent high-frequency roll off in magnitude and phase that can be attributed to motor dynamics, structural dynamics, and on-board sensor filtering. A time-delay was also included in each axis that accounts for sensor and processing delays.

Although only the lateral and directional hover system identification results are presented, modeling of all four axes have been completed. The identified lateral dynamics are overlaid with flight data in Figure 10. As can be seen by the unstable phase rise, the lateral axis is dominated by an unstable hovering cubic between 3 to 4 rad/sec. A similar comparison for the directional axis is shown in Figure 11. It can be seen that the directional axis has a classic K/s shape at low frequency with additional dynamics above 10 rad/sec. These dynamics were modeled as lead/lags and captured torque transfer from the rotors to the airframe and the associated motor dynamics.

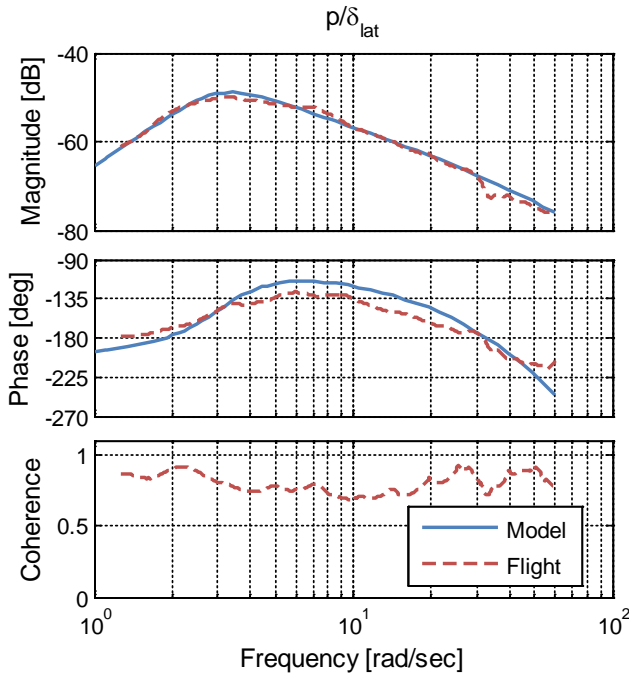


Figure 10. Comparison of lateral bare-airframe model vs. flight data.

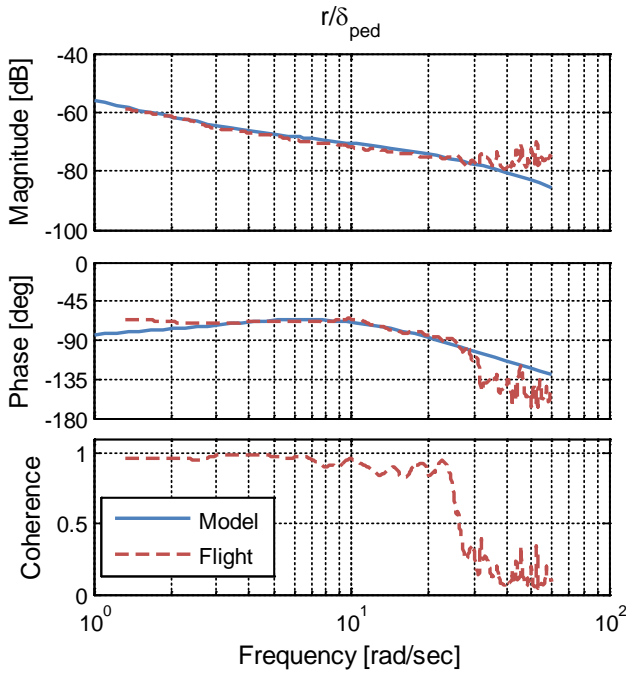


Figure 11. Comparison of directional bare-airframe model vs. flight data.

The identified model parameters for the lateral axis are given in Table 1 along with their Cramér-Rao bounds (CR) and insensitivities (Ref. 7). All parameters are well identified with low Cramér-Rao bounds and insensitivities, giving a

high confidence in the physical parameters of the model. The roll-rate damping derivative (L_p) has a negligible influence on the model and was eliminated from the identification. The identification has an average cost (J_{ave}) of 40, which is well below the $J_{ave} < 100$ threshold (Ref. 7), meaning an accurate model has been obtained.

Table 1. CIFER[®] identified model parameters for lateral axis.

Engineering Symbol	Value	CR [%]	Insensitivity [%]
Y_v	-0.2672	5.75	1.84
L_v	-0.9051	5.68	1.59
L_p^a	0	-	-
$L_{\delta_{lat}}$	0.01471	3.57	1.18
lat^b	50	-	-
τ	0.031	6.33	3.15

^a : eliminated parameter

^b : fixed parameter

The lateral response eigenvalues are obtained from the identified lateral parameters of Table 1. The eigenvalues are comprised of the lateral hovering cubic, which is a characteristic of rotorcraft, and consists of an unstable oscillatory pole and a stable first order pole, both of which are shown in Table 2. The time to double for the unstable mode is $\tau_{double} = 0.48$ sec, which indicates a fast divergent oscillation. Finally, there is a first-order model at high frequency (50 rad/sec) associated with the small electric motor lag.

Table 2. CIFER[®] identified modes for lateral axis.

Mode	Frequency [rad/sec]	Damping	Time to Double/Half [sec]
Unstable Oscillatory Mode	3.03	-0.48	0.48
Stable Mode	3.17	-	0.22
Lag	50	-	0.013

Flight Control Design and Optimization

The stock control laws for the IRIS+ fly reasonably well, but are overly complex and unnecessarily nonlinear. The stock control laws have a PID structure for the inner rate-loop, but the attitude command system has additional nonlinearities such as trigonometric functions and square root controller functions that do not linearize correctly and, as such, do not lend themselves to classical control design methodology. For the project, two simple design architectures, Explicit Model

Following (EMF) and Dynamic Inversion (DI), both of which are representative of state-of-the-art full-size and mid-size rotorcraft control law architectures, were chosen to replace the stock control laws. These control laws were designed using an optimization-based approach embodied in the CONDUIT[®] software and described in detail in Ref. 9.

The EMF architecture for the lateral axis is shown in Figure 12, where the other control axes have a similar architecture. The EMF control law has a command model and a low-order inverse in the feed-forward path, and PID type feedbacks. In contrast, the DI control law, shown in Figure 13, has only a command model in the feed-forward path, and a dynamic inverse that is performed with feedback in the inner-most loop of the control law (via the $[CA]$ and $[CB]^{-1}$ blocks shown in Figure 13). Similar to the EMF, the DI feedback is also a PID-type controller.

For both DI and EMF, the inverse plant models are based on the system identification models described in the previous section (Table 1 for the lateral axis, for instance) and, as such,

are not tuned as part of the control law design. The feedback gains in the PID-like “Feedback” blocks of Figure 12 and Figure 13 were optimized using CONDUIT[®] to meet desired stability, tracking, and disturbance rejection criteria, while minimizing control usage (i.e., crossover frequency and actuator activity). These design criteria were selected from prior experience with full-scale aircraft (Ref. 9), but with modified Level 1/Level 2 boundaries more appropriate for small-scale aircraft in certain specifications. In the case of disturbance rejection bandwidth (DRB) and crossover frequency, the minimum Level 1 requirement was not known for this class of vehicles. Therefore, an optimization strategy known as Design Margin Optimization (DMO, Ref. 9) was used in CONDUIT[®] to incrementally improve the design in order to generate a family of optimized designs. These optimized designs were then tested in indoor flights to determine if performance and tracking would be sufficient during the flight testing reported herein.

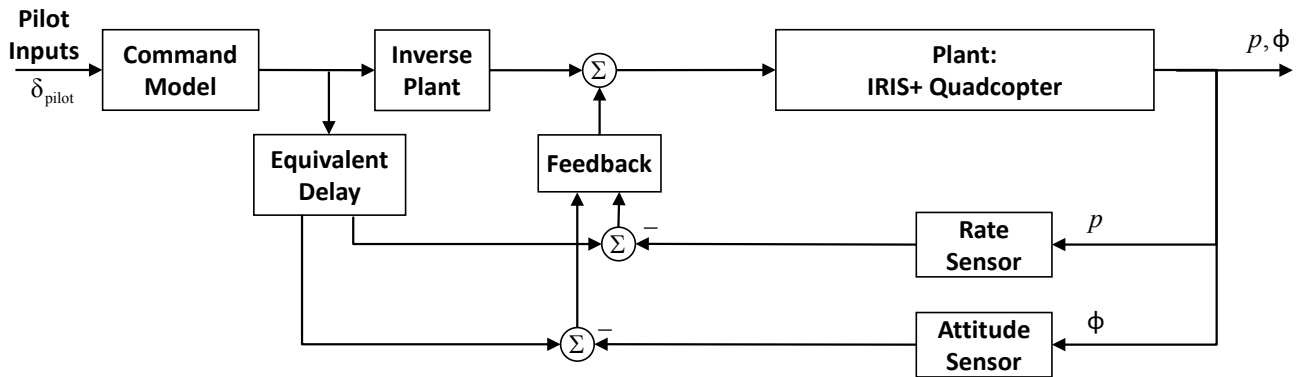


Figure 12. Lateral-axis Explicit Model Following control law architecture.

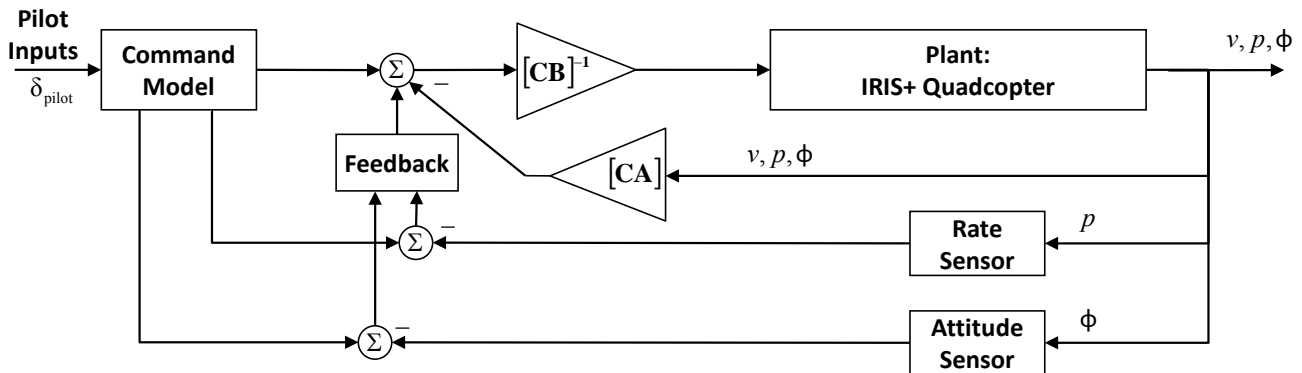


Figure 13. Lateral-axis Dynamic Inversion control law architecture.

Similarly, the piloted bandwidth requirements were not known for this small-scale, remotely piloted aircraft. As such, a minimum piloted bandwidth of 8 rad/sec was chosen for the optimization, which seemed acceptable to the aircraft operators. More investigation in this area is warranted. Outdoor testing in Phase 2 should provide additional data and guidance for these specifications.

A summary of design criteria (specifications) defined for the CONDUIT[®] optimization is shown in Table 3. Detailed explanation of the CONDUIT[®] optimization constraint types and their role in the optimization process are discussed in Ref. 9. In short, during the CONDUIT[®] optimization, the design parameters are automatically tuned to first meet the hard constraints to ensure stability. Once these constraints are met, the optimization works to meet the soft constraints, which typically are performance-based specifications like Disturbance Rejection Bandwidth (DRB), while maintaining Level 1 performance on the hard constraints. Finally, once all the hard and soft constraints are met, summed objectives are minimized to reduce actuator activity and prevent overdesign, while continuing to maintain Level 1 performance on the hard and soft constraints, until an optimized solution is achieved. The optimization strategies were chosen as appropriate for each architecture (Ref. 9).

Sample comparisons between the two different control designs are shown in Table 4 for stability margins, crossover frequency, and DRB. In the DI design methodology, the high fidelity (full-order) inverse plant sets the inner-loop crossover frequency, and is assumed to provide the appropriate level of feedback to give the desired response tracking. Since the control law designs were conducted for Phase 1 of the project which focused on indoor flights and performance, the DI approach was to keep the gains only as high as needed to provide good flying qualities indoors, relying on the dynamic inverse to provide good tracking, as indicated by the lower values for crossover frequency and disturbance rejection.

In contrast, the EMF design methodology, which only uses a low-order inverse, relies on the feedback to correct the inverse model discrepancies. The EMF optimization approach was to maximize disturbance rejection, and, as such, larger disturbance rejection and crossover frequencies were used, at the cost of higher control usage. In outdoor flights, where winds and turbulence are present, the DRB and crossover frequencies will likely need to be increased for the DI design, but the current values were found to be acceptable for the indoor testing phase of the project.

Table 3. Design specifications for CONDUIT[®] optimization.

<i>Specification (CONDUIT[®] name)</i>	<i>Constraint Type</i>	<i>Standard Boundaries?</i>	<i>Comments</i>
Eigenvalues (EigLcG1)	Hard	Y	
Stability Margins (StbMgG1)	Hard	Y	
Nichols Margins (NicMgG1)	Hard	Y	
Disturbance Rejection Bandwidth (DstBwG1)	Soft	N	Minimum Level 1/Level 2 boundary set at 2 rad/sec for all axes, DMO implemented to incrementally increase Level 1 requirement.
Disturbance Rejection Peak Magnitude (DstPkG1)	Soft	Y	
Piloted Bandwidth (BnwAtH2)	Soft	N	Piloted bandwidth Level 1/Level 2 boundary set to 8 rad/sec.
Minimum Crossover Frequency (CrsMnG2)	Soft	N	Minimum Level 1/Level 2 boundary set at 10 rad/sec for all axes, DMO implemented to incrementally increase Level 1 requirement.
Model Following (ModFoG2)	Soft	Y	
Crossover Frequency (CrsLnG1)	Summed Objective	N	Level 1 value increased to accommodate higher frequency
Actuator RMS (RmsAcG1)	Summed Objective	Y	

Table 4. Comparison of control law designs (lateral axis).

	<i>Gain Margin</i> [dB]	<i>Phase Margin</i> [deg]	<i>Crossover Frequency</i> [rad/sec]	<i>DRB</i> [rad/sec]
DI	8.0	41.1	12.3	2.3
EMF	11.2	42.0	31.6	10.2

The applied design optimization strategy has demonstrated that the process used to optimize full-size vehicles scales well to these small-size Group 1 UAS, using the same design requirements, but with some modified boundaries as appropriate for small-scale vehicles. In addition, this methodology is highly time efficient and provides a family of designs with incrementally increasing performance via Design Margin Optimization. Having a family of optimized designs readily available for flight test studies, especially for this class of small-scale aircraft where the Level 1 requirements for some design criteria are not known, is invaluable since they can be easily evaluated to assess performance in flight.

Software- and Hardware-in-the Loop Simulations

After the control laws were developed, and whenever significant modifications were made, both software-in-the-loop (SIL) and hardware-in-the-loop (HIL) simulations were conducted to verify that the control laws were implemented properly.

The ADD-developed desktop simulation software, RIPTIDE (Real-time Interactive Prototype Technology

Integration/Development Environment, Ref. 21), was utilized as the SIL simulation environment for testing the aircraft response to pilot inputs to detect obvious errors, such as sign conventions or unexpected nonlinearities. The Simulink® analysis model was compiled and loaded into RIPTIDE, and a USB sidestick was used to send pilot commands to the simulation environment. The visual output was observed to check for obvious errors prior to testing in HIL simulation.

The HIL simulation was developed to verify that the flight software was properly compiled and uploaded to the Pixhawk flight controller, using the “pictures-to-code” process described in the earlier sections, and was correctly integrated with the IRIS+ hardware. It also allowed the pilot to verify that the system was controllable and exhibited expected behavior. This piloted HIL simulation was necessary because the analysis model did not include mixer nonlinearities or failure modes, and, in some instances, utilized radio control (RC) inputs and sensor outputs with sign conventions, units, and trim values that differed from those collected by the flight software. HIL simulation was also utilized as a means to provide a safe environment for practicing and scaling test maneuvers to verify that the maneuvers performed would not violate airspace restrictions in actual flights, to identify mode switching transients, and to increase and maintain pilot proficiency.

Figure 14 illustrates how the HIL simulation environment communicates among the various hardware and software components.

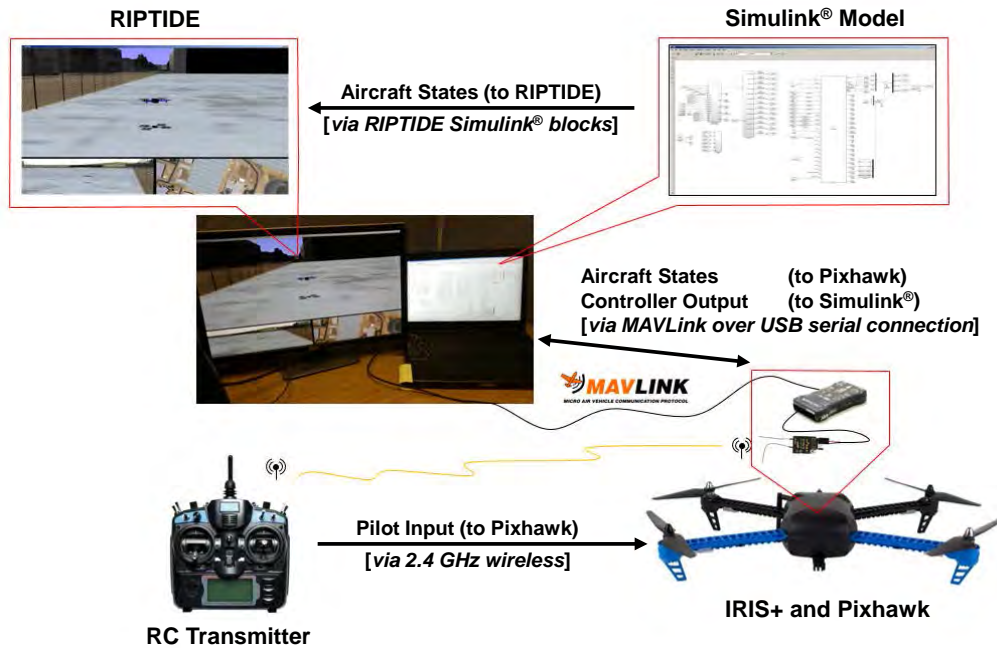


Figure 14. Hardware-in-the-loop communication.

The HIL simulation is implemented such that the flight software running on the Pixhawk flight controller receives pilot commands from a RC transmitter (via a 2.4 GHz RC link), and aircraft state information from the bare-airframe model in Simulink® (via a USB serial connection using MAVLink protocol). The mixer inputs are then transmitted from the control law output to the bare-airframe model (again via a USB serial connection using MAVLink protocol). The aircraft states are also simultaneously sent to RIPTIDE to simulate and display the aircraft motion.

As part of the verification process, the broken-loop and closed-loop responses generated from the analysis model in CONDUIT® are compared to the corresponding responses extracted from automated sweeps in the HIL simulation to verify that the controller has been implemented correctly on the aircraft. If any deficiencies or errors are found, the software is then updated and the verification process is repeated until desired and expected performance are met. Such a verification process provides confidence that the vehicle will perform as expected in flight. Figure 15 shows an example comparison between the broken-loop response extracted from indoor flight data and that extracted from the HIL simulation for the longitudinal axis in the IRIS+ stock “Stabilize” mode. It can be seen that the responses are in good agreement over the frequency range of interest (1 to 30 rad/sec), indicating that the HIL simulation is an accurate representation of the actual aircraft.

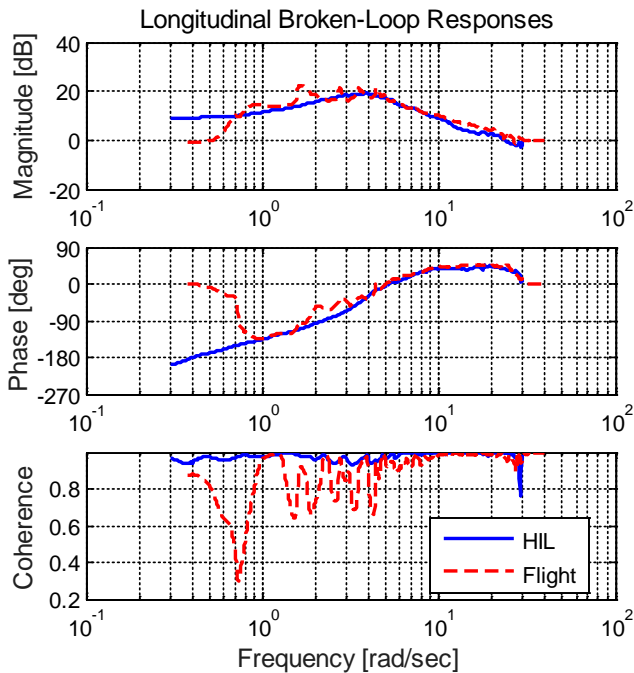


Figure 15. Flight vs. HIL comparison of longitudinal broken-loop response in “Stabilize” mode.

Flight Test and Validation

Having developed and optimized the control laws for the vehicle, and verified them using the HIL simulation, the next step was to conduct flight tests to verify that the design performance was realized in flight. As discussed in previous sections, in Phase 1, the optimized control laws were flown and evaluated indoors. Automated frequency sweep testing was performed to evaluate performance based on design metrics for stability, disturbance rejection, and closed-loop response. The sweeps were injected with manual pilot inputs active, allowing small corrections to be made as necessary. Currently, in Phase 2, some outdoor tethered frequency sweep testing has been conducted. In both cases, where piloted inputs were made during the sweeps, care was taken to ensure the inputs were small and uncorrelated with the sweep inputs.

The broken-loop stability was evaluated by injecting automated frequency sweeps at the plant model (labeled “Broken-loop Inputs” as indicated in Figure 16 for the EMF architecture), typically in the 0.2 to 40 rad/sec range. The broken-loop response was used to determine the crossover frequency along with the stability margins. The disturbance rejection was evaluated using automated sweeps injected at the relevant sensor output, based on the DRB metric (Ref. 22). For example, in the lateral axis, as shown in Figure 16, a sweep is inserted at the roll attitude sensor output (ϕ_m) and the frequency response, ϕ'/ϕ_d , is computed between the total (ϕ') and disturbance inputs (ϕ_d). Finally, the closed-loop performance was computed using sweeps (either automated or piloted) applied at the pilot input to the control laws.

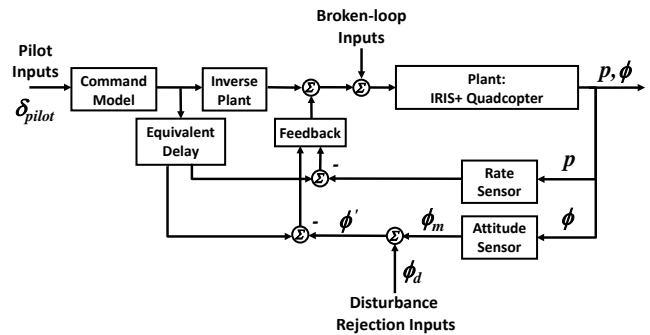


Figure 16. Location of various lateral sweep inputs for EMF architecture.

The frequency responses in each case were extracted from flight test data using CIFER®. Figure 17 is an example of the lateral broken-loop frequency response comparison plot for the design and indoor flight test performance, based on the DI control laws. The gain margin (GM) and phase margin (PM), as well as the crossover frequency, are marked on the figure. Within the frequency range of interest (approximately 2 to 30 rad/sec), the design and flight test broken-loop responses have excellent agreement, which validates the

implementation of the control laws onto the IRIS+ and the identified bare-airframe model.

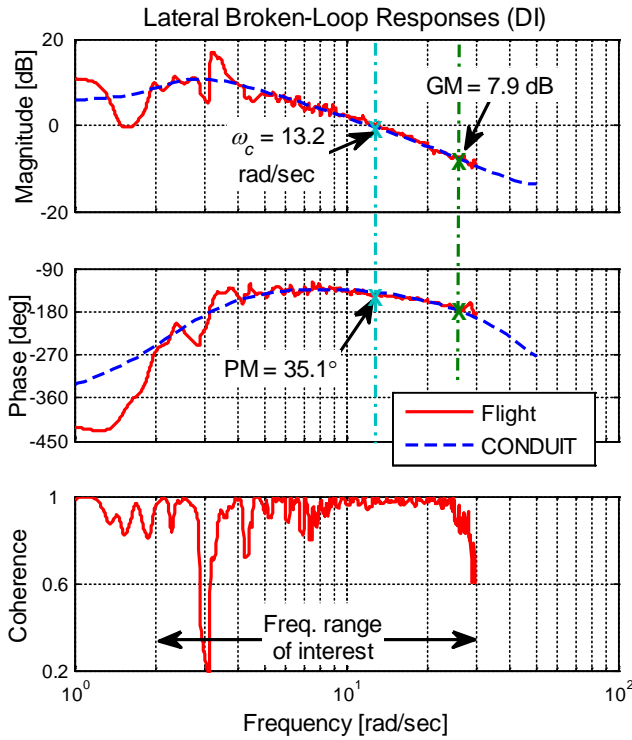


Figure 17. Example lateral broken-loop response comparison for DI architecture.

An example comparison of the lateral closed-loop response for the EMF architecture is shown in Figure 18. As was the case for the broken-loop response, the design and flight test closed-loop performance match well. Similarly, an example comparison of the lateral disturbance rejection response for the EMF architecture is shown in Figure 19 and indicates good predictive capability, as exemplified for the EMF controller up to 30 to 50 rad/sec.

These frequency response comparisons provide confidence that the analysis model correctly predicts flight behavior over the frequency range of interest for both the EMF and DI control architectures.

A comparison of the design and flight test metrics is presented in Table 5 for the DI and EMF control law architectures in the lateral axis. The values of the design metrics shown here for both the DI and EMF architectures are the same as the ones presented in Table 4. Also shown are the flight test values for the stock IRIS+ “Stabilize” mode. As can be seen, for each design, the flight test and design values agree well for most metrics, with the exception of a small reduction in the phase margin in the flight test. This is most likely the result of small discrepancies between the phase of the model and the actual vehicle response in the region of the crossover

frequency, as can be seen in Figure 10. Also note that there is no gain margin reported for the EMF control laws since the broken-loop frequency sweep was not conducted to a high enough frequency to capture the 180 deg crossing for gain margin determination.

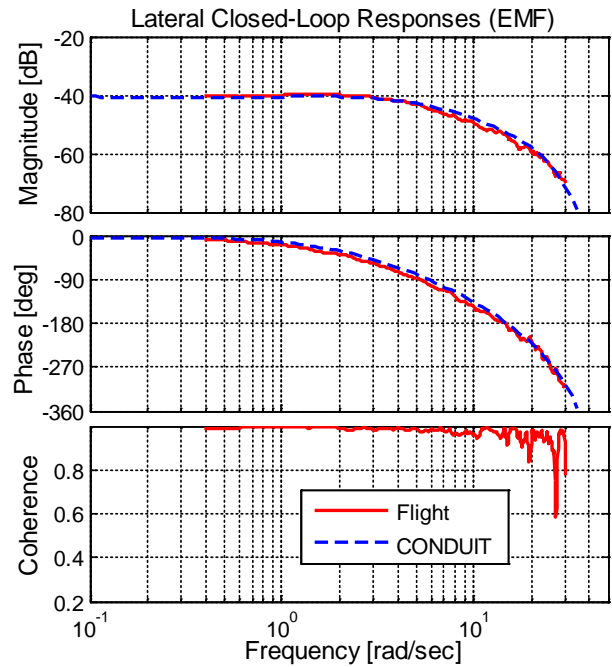


Figure 18. Example lateral closed-loop response comparison for EMF architecture.

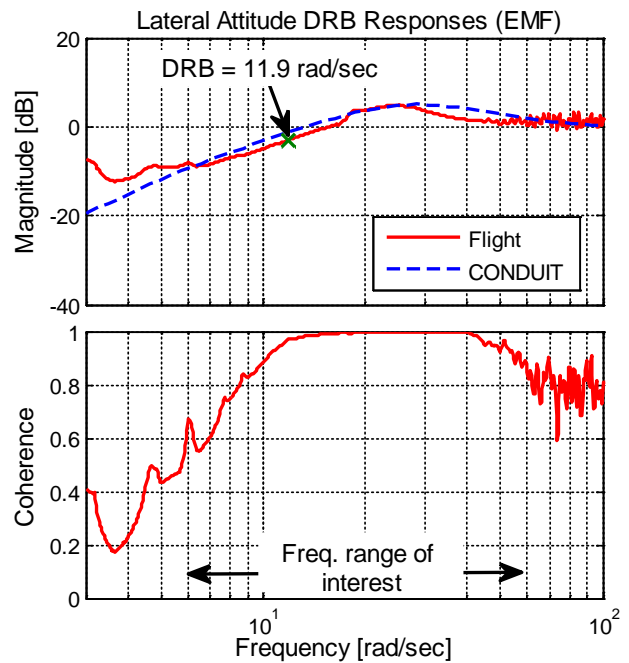


Figure 19. Example lateral attitude DRB response comparison for EMF architecture.

Table 5. Comparison of lateral axis design and flight test performance metrics.

	<i>Gain Margin [dB]</i>		<i>Phase Margin [deg]</i>		<i>Crossover Frequency [rad/sec]</i>		<i>DRB [rad/sec]</i>	
	Flight	Design	Flight	Design	Flight	Design	Flight	Design
DI	7.9	8.0	35.1	41.1	13.2	12.3	2.0	2.3
EMF	-	11.2	34.0	42.0	32.8	31.6	11.9	10.2
“Stabilize”	5.3	-	32.8	-	30.9	-	7.5	-

Also, as can be seen in Table 5, while the EMF controller design has similar DRB and crossover characteristics in flight as the stock “Stabilize” mode, significant variations in DRB and crossover frequency are evident between the DI and EMF designs. As explained in the control design section earlier, the design approach for each was quite different, where the DI design took a more conservative approach to accomplish primarily the Phase 1 indoor mission, while the EMF design was more aggressive in trying to maximize DRB performance.

Performance Metrics for Full-scale vs. Small-scale Vehicles

The difference between the design approaches described above, as well as the need to adjust some performance specifications during the design process, brings up a key point that the current specifications utilized for control law development herein are based primarily on larger scale aircraft, and are not necessarily directly applicable to small-scale vehicles. As a comparison, shown in Table 6 are the lateral-axis flight test values for the three IRIS+ control laws, along with typical values from a UH-60 flight test using

advanced cable angle/rate feedback (CAF) control laws of similar complexity (Ref. 23).

The crossover frequency, DRB, and piloted bandwidth for the small-scale IRIS+ all vary significantly from the full-scale UH-60 data. For this reason, flight-testing formed an integral part of the design process in order to establish “reasonable” design specification boundaries for a small-scale vehicle. This was particularly the case for the closed-loop bandwidth, which to a large extent was evaluated with reference to the “Stabilize” mode. As mentioned previously, the final DRB and crossover values were established based on DMO results, which effectively represented the physical limitations of the system rather than actual performance requirements. This process was necessary due to the absence of suitable small-scale design boundaries, and highlights the need for an objective assessment of small-scale flight control requirements.

Table 6. Comparison of lateral axis flight control metrics between IRIS+ and UH-60.

	<i>Gain Margin [dB]</i>	<i>Phase Margin [deg]</i>	<i>Crossover Frequency [rad/sec]</i>	<i>DRB [rad/sec]</i>	<i>Piloted Bandwidth [rad/sec]</i>
DI	7.9	35.1	13.2	2.0	7.0
EMF	-	34.0	32.8	11.9	9.5
“Stabilize”	5.3	32.8	30.9	7.5	10.2
UH-60 CAF	6.78	47.55	4.69	2.24	3.2

SCORING METRICS DEVELOPMENT

Mission-based scoring and benchmarking metrics are being formulated as part of the Phase 2 research missions to provide a consistent and reliable process to quantitatively evaluate and compare the performance of the two control designs in flight. A selective set of ADS-33 MTE maneuvers, including, but not limited to, hover, pirouette, depart/abort, and slalom, has been identified as relevant maneuvers that can be used to demonstrate the various performance aspects achieved by the control designs. Since many of the ADS-33 MTEs are designed for full-size rotorcraft, these MTEs need to be kinematically scaled so that they are suitable for the much smaller size IRIS+. In addition to the scaled ADS-33 trajectories, a set of recorded trajectories generated from flight tests of the Obstacle Field Navigation (OFN) software will also be used as part of the flight missions. These trajectories include more challenging tasks like sudden stops and swerves to avoid obstacles which are practical missions that the small-scale vehicles are expected to achieve. These maneuvers will be available as commanded trajectory files which will be uploaded to the IRIS+ before flight so that they can be flown autonomously.

For each maneuver, the control laws will be evaluated based on three metrics: aggressiveness, tracking, and robustness. For evaluating aggressiveness and tracking, a given maneuver will initially be flown at a low level of aggressiveness. The maneuvers will then be repeated with increasing level of aggressiveness, until the safety pilot or safety monitor determines higher aggressiveness is not advisable. For measuring robustness, a maneuver with fixed aggressiveness level will be flown dozens of times. Any safety pilot disengagement or other control anomalies will count against the robustness score. Increased aggressiveness, decreased tracking error, and increased robustness will each contribute to an improved score.

The scoring metric determines the performance of a flown trajectory against the commanded trajectory. The scoring objective function, L , is given by a weighted sum of the individual objectives for aggressiveness (α), tracking performance (ε), and robustness (R):

$$L = w_\alpha \frac{\alpha - \alpha_G}{\alpha_B - \alpha_G} + w_\varepsilon \frac{\varepsilon - \varepsilon_G}{\varepsilon_B - \varepsilon_G} + w_R \frac{R - R_G}{R_B - R_G} \quad (2)$$

The weights, w_α , w_ε , and w_R , in Eq. 2 determine the relative importance of the individual objectives. For each individual objective metric, the conditioning parameter with a subscript B (α_B , for instance) stands for the “bad” or worst possible value for the metric, whereas the conditioning parameter with a subscript G (α_G , for instance) stands for the “good” or best possible value. These conditioning parameters are used to normalize the score of each metric, similar to the numerical handling-qualities scoring approach used in

CONDUIT® (Ref. 9). The three variables in Eq. 2 are defined as:

- α : aggressiveness is defined as the ratio of the maximum commanded speed in the scaled trajectory ($V_{max,cmd}$) to the maximum speed in the unscaled trajectory (V_{nom}):

$$\alpha = \frac{V_{max,cmd}}{V_{nom}} \quad (3)$$

- ε : tracking error is defined as the weighted sum of the normalized velocity and position errors. The normalized velocity error is calculated by scaling the root-mean-square error (RMSE) of velocity (vel) by the maximum commanded speed ($V_{max,cmd}$). Similarly, the normalized position error is calculated by scaling the RMSE of position (pos) by the maximum commanded distance from the starting point of the trajectory (L_{path}).

$$\varepsilon = w_{vel} \frac{RMSE(vel)}{V_{max,cmd}} + w_{pos} \frac{RMSE(pos)}{L_{path}} \quad (4)$$

- R : robustness is defined as the ratio of the number of successful flights to the total number of flights:

$$R = \frac{N_{success}}{N_{flights}} \quad (5)$$

Based on the weighted sum of the three metrics (Eq. 2), the objective function L is mapped to a 0-100 scale to determine the final score, Φ :

$$\Phi(L) = \frac{200}{1+e^L} \quad (6)$$

This mapping is defined such that minimizing L will maximize the final score, and a value of $L=0$ will result in a perfect score of 100.

Aside from the scaled ADS-33 MTEs and pre-recorded OFN trajectories, a dedicated hover hold task will also be included as part of the evaluation mission. The aforementioned turbulence arena setup will be used to assess how well each design can hold position within specified bounds for a specific length of time. Since the fan speed can be varied through the use of the variable frequency drive, similar aggressiveness and position tracking metrics can be employed to evaluate the hover hold capability of the designs.

The final formulation of the scoring metrics is currently underway. Simulation and outdoor maneuver data will be collected and analyzed to determine the proper scaling of the ADS-33 MTEs as well as the values for the weights and conditioning parameters. The baseline aggressiveness level for each maneuver will also be determined.

TURBULENCE MODELING AND DISTURBANCE REJECTION RESEARCH

As part of the Quadrotor GNC project research activities, dedicated effort was spent on the development of a turbulence model suitable for small-scale quadrotors like the IRIS+. The model was used to assess disturbance rejection capability in simulation, and drive the design of a performance-based disturbance rejection flight control system in which root mean square (RMS) attitude and position errors due to CETI turbulence were key performance metrics.

CETI Turbulence Modeling

A turbulence model based on the Control Equivalent Turbulence Input (CETI) (Ref. 15, Ref. 16) was developed for the IRIS+. Detailed discussion of the development of this CETI model can be found in Ref. 14. The CETI model uses flight data taken in turbulence to reproduce control inputs needed to generate the same levels of motion as were seen during the flight in turbulence. The turbulence model extraction process requires an accurate model of the bare-airframe, which was obtained using the system identification approach described in the earlier section. Figure 20 illustrates how the extracted CETI model is used to inject turbulence (δ_t) to the control system to simulate the presence of turbulence.

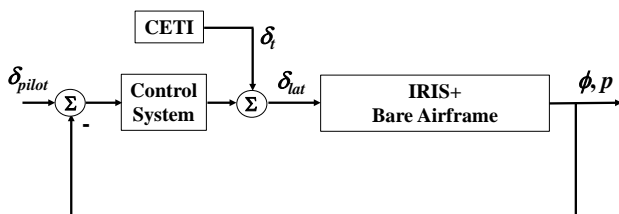


Figure 20. Schematic block diagram of IRIS+ control system with CETI input.

As discussed in Ref. 14, a sample application was developed to simulate and compare the performance of a control system that is similar to the stock "Stabilize" mode ("Baseline Sim") and its optimized solution with high disturbance rejection bandwidth ("Optimized Sim") against the stock IRIS+ "Stabilize" mode flight data taken in turbulence. When the extracted CETI model is coupled back into a simulation of the IRIS+ with the "Baseline Sim" control system, the overall aircraft motion generated using the CETI model matches well with flight data, as shown in Figure 21. This lent confidence in the accuracy of the model. The turbulence model was then applied to the new control laws. As can also be seen from Figure 21, the more aggressive control system is able to reduce the oscillations resulting from turbulence.

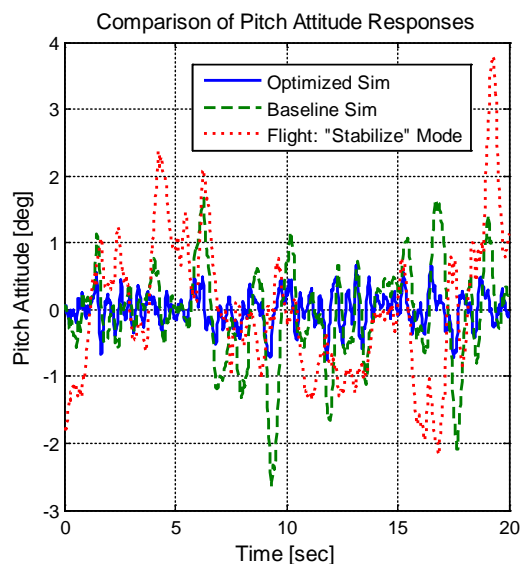


Figure 21. Comparison of pitch attitude time histories between two simulated control systems and flight data.

Performance-Based Disturbance Rejection Flight Control Design

In conjunction with the CETI model development, research was conducted to assess the use of performance-based disturbance rejection requirements to drive the design of a flight control system for UAS like the IRIS+. A summary of the research is provided here, while more details of this study can be found in Ref. 17.

Using the EMF architecture as the basis of this design, an attitude-command/attitude-hold (ACAH) control system with position-hold (PH) capability was designed to aggressively maintain trim attitude and hold a position over the ground in the presence of turbulence and wind gusts. Performance-based disturbance rejection requirements that bound the attitude and position errors due to CETI turbulence to within three times the corresponding RMS values ($3 \cdot \text{RMS}$), and bound the maximum position excursion due to a 1-cosine gust, were used to drive the control system design. In addition, the control system was designed to meet a comprehensive set of stability and flying-qualities specifications. The developed CETI turbulence model was used to simulate turbulence in flight and assess the disturbance rejection performance of the designed system.

Figure 22 shows the pitch attitude error response (θ_{err}) of the IRIS+ subjected to CETI turbulence in flight for two ACAH control systems. The first control system uses the proposed performance-based disturbance rejection design philosophy which imposed a requirement of $3 \cdot \text{RMS}(\theta_{err}) \leq 2$ deg on the aircraft's pitch attitude error. The second controller is that of the stock "Stabilize" attitude control system. Using the performance-based design allowed for a factor of 3.5

improvement in pitch attitude disturbance rejection when subjected to CETI turbulence.

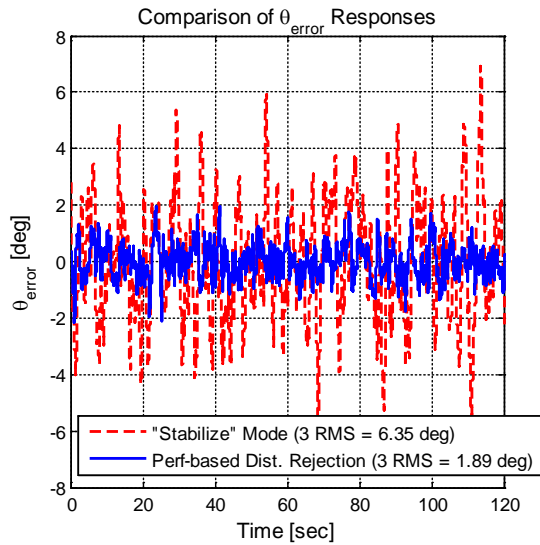


Figure 22. Pitch attitude error response to CETI turbulence.

Figure 23 shows the position response of the IRIS+, from flight data, when subjected to CETI turbulence in 2 to 3 knot winds for two PH control systems. The performance-based design imposed requirements of $3 \cdot \text{RMS}(x_{err}) \leq 0.61$ ft and $3 \cdot \text{RMS}(y_{err}) \leq 0.51$ ft on the aircraft’s position errors when simultaneously subjected to CETI turbulence and a 10 knot 1-cosine gust. The second controller is that of the stock “Loiter” control system, which is a position hold controller wrapped around the stock “Stabilize” attitude control system. Using the performance-based design, the IRIS+ was able to maintain its position within a 3.5 in. radius, allowing for over a factor of 10 improvement in position disturbance rejection when compared to the stock control system.

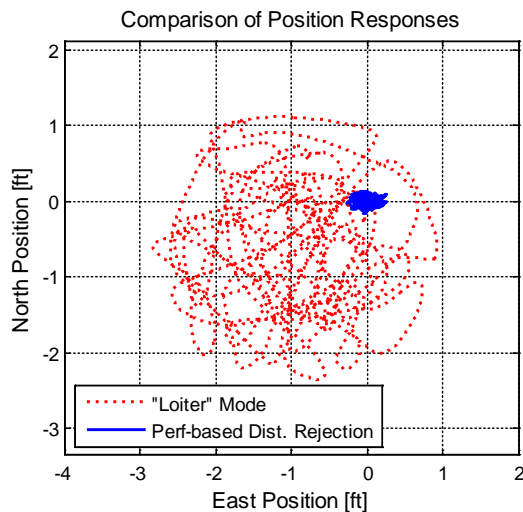


Figure 23. Position response to CETI turbulence.

NEXT STEPS

As the project recently transitioned to Phase 2 with the approvals obtained for flying the IRIS+ outdoors at Ames and Moffett Federal Airfield, the next step is to complete the outer-loop control law design for both the EMF and DI architectures. Further experimentation will be conducted outdoors to determine if the optical flow and LIDAR sensor system is necessary to obtain more precise position information than the on-board GPS can provide, with the goal of achieving better performance for position hold related tasks. Once additional simulation and flight test data are collected, the applicable set of ADS-33 MTEs will be identified and properly scaled for the IRIS+-size vehicles. The scoring metrics will also be formulated for evaluation of the two designs based on aggressiveness, tracking, and robustness. To conclude the project, an outdoor fly-off demonstration event will be held at the Moffett Federal Airfield, where the two designs will be performing the hover hold task and flying the scaled ADS-33 MTEs and recorded OFN trajectories with increasing level of aggressiveness, and will be scored accordingly.

FUTURE APPLICATIONS

In future work, ADD seeks to apply the technologies demonstrated herein for the quadrotor to a range of emerging multi-rotor concepts. A key DoD program is the Future Tactical UAS (FTUAS), which will develop a family of runway independent (Vertical Take-off and Landing, VTOL) UAS spanning the range of weight groups for various applications (Ref. 24). Another emerging technology is the Distributed Electrical Propulsion (DEP, Ref. 25), which uses an array of electrically-powered rotors along a wing in a “blown flap configuration” – similar to the NASA Quiet Short-Haul Research Aircraft (QSRA, Ref. 26). This provides a significant increase in the lift-to-drag ratio for longer range, with a much smaller and lighter wing. Finally, there is a family of new “tail sitter” concepts (the joint DARPA and U.S. Navy TERN program, Ref. 27, for instance) that have a VTOL capability for runway independence, but quickly transition to a lifting wing for long range. Each of these configuration types poses its own challenges, but ADD expects that the technology demonstrated herein can be adapted to demonstrate improved mission effectiveness and development efficiency in a more methodical development process.

CONCLUSIONS

The Quadrotor Guidance, Navigation, and Control project has been developed to apply ADD’s advanced flight control technologies from full-size conventional aircraft to small-scale multi-rotor vehicles like the IRIS+. It has been demonstrated that the ADD “desktop-to-flight” development workflow and the associated engineering methodologies can

be successfully adapted and applied to these small-size vehicles. The following conclusions are made:

1. Frequency-domain-based system identification methodologies and tool (CIFER[®]), which are widely used for identification of dynamic models for full-size aircraft, can be applied to extract an accurate model of a small-scale quadrotor like the IRIS+. The identified low-order dynamic model accurately tracks the unstable dynamics over a wide frequency range of interest, even with the presence of noisy signals in the frequency sweep data used for the identification process.
2. Commonly used control law architectures like Explicit Model Following and Dynamic Inversion found in many full-size aircraft have shown to be equally well suited for UAVs. All the typical design requirements and optimization strategies for full-size aircraft can be applied using CONDUIT[®] to design these control laws for a much smaller scale vehicle and achieve excellent dynamic response characteristics and explore the optimization trade-offs.
3. Although full-size rotorcraft optimization strategies and the same design metrics well characterize the response of the quadrotor UAV, adjustments to the Level 1/Level 2 boundaries of many of the performance metrics (DRB, bandwidth, crossover frequency) were required to scale the requirements appropriately to meet the desired performance of the much smaller IRIS+. The key metrics are appropriate but the boundaries must be significantly tightened in comparison to full-scale aircraft. Therefore, there is a need to develop a revised set of “handling qualities” performance specifications that are more applicable to small-scale vehicles.
4. Given that the minimum Level 1 requirement for some key performance metrics like DRB and crossover frequency are not yet known for this class of vehicles, the Design Margin Optimization capability in CONDUIT[®] can significantly reduce the need for an iterative design process, as a family of incrementally improved optimized designs can be easily generated and evaluated in flight.
5. The CETI model developed for the IRIS+ has been demonstrated to simulate realistic turbulence for small UAVs. This model can serve as an essential tool for performing control law analysis and trade-off studies to assess disturbance rejection performance in simulation and in flight. In addition, the CETI model was used to drive the design of a performance-based disturbance rejection flight control system. This performance driven design achieved significant improvements in the aircraft’s ability to hold a position when subjected to CETI turbulence in flight over the stock control system.

ACKNOWLEDGMENTS

The Quadrotor GNC project team would like to express our sincere appreciation to Professor Juan Alonso at Stanford University for the many excellent ideas he provided during the planning and deployment of this project. His experience and suggestions based on many years of experience teaching the “Design, Construction, and Testing of Autonomous Aircraft” course (AA241X) at Stanford University served as a model for this project. Professor Alonso also serves as a formal advisor to the project, providing excellent feedback and mentorship. The team would also like to thank our ADD colleagues: Dr. Mark Tischler, Mr. Matthew Whalley, Dr. Marc Takahashi, and Mr. Christopher Blanken who also serve as advisors to the project, and Dr. Samuel Huang for his dedicated assistance with the COA application and flight readiness approval process. A special thank you also goes to Mr. Evan Ivler for his voluntary assistance in designing and fabricating the custom mount for the optical flow and LIDAR sensor system.

REFERENCES

- ¹U.S. Army, “U.S. Army Unmanned Aircraft Systems Roadmap 2010-2035,” Progressive Management, December 2010.
- ²Kloet, N., Watkins, S., and Clothier, R., “Acoustic signature measurement of small multi-rotor unmanned aircraft systems,” *International Journal of Micro Air Vehicles*, 0 (0), January 2017, pp. 1-12.
- ³Weiss, E., “UPS Tested Launching A Drone From A Truck For Deliveries,” USA Today, February 21, 2017.
- ⁴D’Agata, C., “ISIS Drones Pose Another Danger as Iraqi Troops Push For Western Mosul,” CBS News, February 20, 2017.
- ⁵Anon., “Photos show ‘weaponised commercial drones’ in Iraq,” BBC News Online, January 18, 2017.
- ⁶Niermeyer, P., Raffler, T., and Holzapfel, F., “Open-Loop Quadrotor Flight Dynamics Identification in Frequency Domain via Closed-Loop Flight Testing,” AIAA SciTech Forum, Kissimmee, FL, January 5-9, 2015.
- ⁷Tischler, M. B., and Remple, R. K., *Aircraft and Rotorcraft System Identification: Engineering Methods and Flight Test Examples, Second Edition*, AIAA, Reston, VA, 2012.
- ⁸Wei, W., Tischler, M. B., and Cohen, K., “System Identification and Controller Optimization of a Quadrotor UAV,” American Helicopter Society 71st Annual Forum Proceedings, Virginia Beach, VA, May 5-7, 2015.

⁹Tischler, M. B., Berger, T., Ivler, C. M., Mansur, M. H., Cheung, K. K., and Soong, J. Y., *Practical Methods for Aircraft and Rotorcraft Flight Control Design: An Optimization-Based Approach*, AIAA, Reston, VA, 2017.

¹⁰Cooper et al., “Vehicle Modeling for Flight Test Measurements of Ship Airwake Disturbances,” American Helicopter Society 72nd Annual Forum Proceedings, West Palm Beach, FL, May 17-19, 2016.

¹¹Anon., “Aeronautical Design Standard, Handling Qualities Requirements For Military Rotorcraft,” USAAMCOM ADS-33E-PRF, U.S. Army Aviation and Missile Command, Huntsville, Alabama, March 2000.

¹²Whalley, M., Takahashi, M., Tsenkov, P., Schulein, G., and Goerzen, C., “Field-Testing of a Helicopter Obstacle Field Navigation and Landing System.” American Helicopter Society 65th Annual Forum Proceedings, Grapevine, TX, May 27-29, 2009.

¹³3D Robotics Inc., *IRIS+ Operation Manual vF*, 3D Robotics, Berkeley, CA, December 2014.

¹⁴Juhasz, O., Lopez, M. J. S., Berrios, M. G., Berger, T., and Tischler, M. B., “Turbulence Modeling of a Small Quadrotor UAS Using System Identification from Flight Data,” AHS Technical Meeting on VTOL Unmanned Aircraft Systems, Mesa, AZ, January 24-26, 2017.

¹⁵Lusardi, J. A., Tischler, M. B., Blanken, C. L., and Labows, S. J., “Empirically Derived Helicopter Response Model and Control System Requirements for Flight in Turbulence,” *Journal of the American Helicopter Society*, July 2004, pp. 340-349.

¹⁶Lusardi, J. A., von Gruenhagen, W., and Seher-Weiss, S., “Parametric Turbulence Modeling for Rotorcraft Applications: Approach, Flight Tests and Verification,” Rotorcraft Handling Qualities Conference, Liverpool, UK, November 2008.

¹⁷Berrios, M. G., Berger, T., Tischler, M. B., Juhasz, O., and Sanders, F. C., “Hover Flight Control Design for UAS using Performance-based Disturbance Rejection Requirements,” American Helicopter Society 73rd Annual Forum Proceedings, Fort Worth, TX, May 2017.

¹⁸R.M. Young Company, *Ultrasonic Anemometer Model 81000 Instructions Manual*, R.M. Young Company, Traverse City, MI, 2004.

¹⁹Meier L., Honegger D., and Pollefeys M., *PX4FLOW-Smart Camera Quick Start-Hardware Version 1.3*, PX4 Autopilot, Berkeley, CA, 2015.

²⁰Garmin, Ltd., *Lidar Lite v3 Operation Manual and Technical Specifications*, Garmin International, Inc., Olathe, KS, 2014.

²¹Anon., *RIPTIDE User’s Guide, Version 2.1*, Universities Space Research Association, Moffett Field, CA, 2015.

²²Berger, T., Ivler, C. M., Berrios, M. G., Tischler, M. B., and Miller, D. G., “Disturbance Rejection Handling Qualities Criteria for Rotorcraft,” American Helicopter Society 72nd Annual Forum Proceedings, West Palm Beach, FL, May 17-19, 2016.

²³Ivler, C. M., Powell, J. D., Tischler, M. B., Fletcher, J. W., and Maj. Ott, C., “Design and Flight Test of a Cable Angle/Rate Feedback Flight Control System for the RASCAL JUH-60 Helicopter,” American Helicopter Society 68th Annual Forum Proceedings, Fort Worth, TX, May 2012.

²⁴Carey, B., “U.S. Services Outline Future Plans for Unmanned Aircraft,” Aviation International News, November 2, 2016.

²⁵Ashley, S., “Flight Propulsion Goes Electric,” SAE International, June 12, 2015.

²⁶Martin, J., “The Quiet Short-Haul Research Aircraft (QSRA),” *Society of Experimental Test Pilots, Technical Review*, Vol. 14, No. 4, 1979, pp. 77-93.

²⁷Anon., “DARPA Doubles Down on Tern by Funding 2nd Test Vehicle,” DARPA Public Affairs (outreach@darpa.mil), November 17, 2016.